



UNIVERSITÀ POLITECNICA DELLE MARCHE
Repository ISTITUZIONALE

Flood impact on masonry buildings: The effect of flow characteristics and incidence angle

This is the peer reviewed version of the following article:

Original

Flood impact on masonry buildings: The effect of flow characteristics and incidence angle / Postacchini, Matteo; Zitti, Gianluca; Giordano, Ersilia; Clementi, Francesco; Darvini, Giovanna; Lenci, Stefano. - In: JOURNAL OF FLUIDS AND STRUCTURES. - ISSN 0889-9746. - STAMPA. - 88:(2019), pp. 48-70. [10.1016/j.jfluidstructs.2019.04.004]

Availability:

This version is available at: 11566/266247 since: 2020-05-08T15:16:04Z

Publisher:

Published

DOI:10.1016/j.jfluidstructs.2019.04.004

Terms of use:

The terms and conditions for the reuse of this version of the manuscript are specified in the publishing policy. The use of copyrighted works requires the consent of the rights' holder (author or publisher). Works made available under a Creative Commons license or a Publisher's custom-made license can be used according to the terms and conditions contained therein. See editor's website for further information and terms and conditions.

This item was downloaded from IRIS Università Politecnica delle Marche (<https://iris.univpm.it>). When citing, please refer to the published version.

(Article begins on next page)

Flood impact on masonry buildings: the effect of flow characteristics and incidence angle

Matteo Postacchini^{a,*}, Gianluca Zitti^a, Ersilia Giordano^a, Francesco Clementi^a, Giovanna Darvini^a, Stefano Lenci^a

^a*Department of ICEA, Università Politecnica delle Marche, Ancona, Italy*

Abstract

Climate change and the raising number of extreme events, such as severe floods, has increased the attention on their effects on urban systems. Urban floods generate important hydrodynamic loads on building and this work proposes a first systematic study on the actions generated by floods with different characteristics (depth, velocity and incidence angle) on masonry buildings. The study is carried out with experimental tests reproducing a masonry bay with scale 1:10, while the effect of the flow hitting the building has been obtained by moving the building in the water at rest. The pressure generated by the fluid at the four walls of the building was recorded using pressure transducers. It has been found that the overpressure acting on the building depends on the flow characteristics in different manner for the frontal, lateral and rear walls. Further, the incidence angle plays a major role in the generation of a pressure gradient along the impacted wall, and significantly affects both peak frequency and spectral energy. Use of theoretical models suggests that (i) the drag coefficient of the building decreases with the Froude number, and only slightly depends on the incidence angle, and (ii) the blocking effect largely affects the hydrodynamics around the structure.

Keywords: urban floods, flow-building interaction, laboratory experiments, flow-incidence angle, hydrodynamics, drag coefficient

1. Introduction

In the last decades, climate changes are significantly increasing the risk of flood and inundation, which, in turn, provide uncertainties in the traditional decision frameworks and management actions (e.g., see Poff et al., 2016). This picture is likely to occur in both coastal and riverine environments (e.g., Ranasinghe et al., 2013; Villatoro et al., 2014; Arnell and Gosling, 2016). In particular,

*Corresponding author

Email address: m.postacchini@univpm.it (Matteo Postacchini)

overbuilding in the proximity of rivers and coasts has increased the flood hazard, since flood-prone areas are more attractive for both people/inhabitants and socioeconomic activities (e.g., de Moel et al., 2009; Braun and Aßheuer, 2011).
 10 Some urban areas have already experienced tragic events, like those recently occurred, among others, in Europe (Raynaud et al., 2015; Faccini et al., 2016; Bernardini et al., 2017), Asia (Duy et al., 2017; Halgamuge and Nirmalathas, 2017), America (Saharia et al., 2017). However, such floods are characterized by large uncertainties, due to the significant variations in the statistics of rain-
 15 fall (or other hydrological variables) at regional and sub-regional scales (e.g., see Kundzewicz et al., 2014; Soldini and Darvini, 2017). Urban floods are also related to the manipulation of natural watersheds. Human activities, like cultivation, irrigation, deforestation or urban construction, can alter the catchment response to precipitation and largely contribute to runoff change (e.g., Memmola
 20 and Darvini, 2018).

A key aspect of the hazard management is the assessment of the damage, which is usually related to the flood characteristics by means of damage curves (Pistrika and Jonkman, 2010; Pistrika et al., 2014; Huizinga et al., 2017; Lee and Kim, 2018). Such curves take into account both water depth and velocity,
 25 and are site-dependent, because of the lack of knowledge on effects of the building characteristics on the building-flow interaction. On the other hand, the diversification of building techniques, procedures and/or components hinders an accurate parameterization of the building characteristics without resulting in a specific study of a singular building (e.g., see Xiao et al., 2013; Custer and
 30 Nishijima, 2015).

In spite of the variety of building techniques, some additional aspects should be considered to improve the damage assessment. Among the flood actions on buildings (Kelman and Spence, 2004), the focus is here on the hydrostatic and hydrodynamic loads and on the aspects affecting these actions. Such loads
 35 are function of the flow characteristics (i.e. water level and velocity), which are taken into account in typical damage assessments, but also of the building and urban fabric features, such as: structure geometry (e.g., square rather than circular cylinders), structure material (e.g., masonry, steel, reinforced concrete; see Suppasri et al., 2013), blocking effect (e.g., due to the relative distance
 40 between buildings).

This work focuses on a construction type typical of the Italian urban fabric, as the one described in Bernardini et al. (2017). Specifically, Italian constructions are commonly masonry buildings and reinforced concrete structures with masonry infill walls, both characterized by scarcely permeable surfaces. Ma-
 45 sonry buildings show a great structural strength (e.g., the buildings survived to hurricane Katrina in Robertson et al., 2007), but literature on flood impact on such construction typology is scarce. In fact, the high stiffness of the structure and the roughness of the external walls are important features affecting the hydrodynamics around the building and, subsequently, the force exerted on it.
 50 Besides the construction type, another peculiar feature is the placement of the buildings in urban fabrics, which are not always regular. Therefore, the flood can hit buildings with different incidence angles also without changing its main

(streamwise) direction (see Figure 1). Therefore, given the construction type, the flood impact can be studied as a function of: water level, water velocity and flow incidence.



Figure 1: Overview of an area of Senigallia (Italy) hit by the flood occurred in May 2014. Some of the buildings which are not perpendicular to the flow are shown in red. The topographic map is adapted from Carta Tecnica Regionale of the Regione Marche (http://ctr.regione.marche.it/marcheCTR_web/default.aspx). The shaded cyan indicates the inundated area, taken from the web site of COPERNICUS EU programme (<http://emergency.copernicus.eu/mapping/list-of-components/EMSR083/GRADING/ALL>).

Floods, like that occurred in Senigallia (Italy) in May 2014, are characterized by slow rising, i.e. steady or quasi-steady conditions within the urban domain (e.g., see Bernardini et al., 2017, where a boundary condition characterized by a water depth $h = 0.8m$ and a flow velocity $v = 2m/s$, which provided a Froude number $Fr = v/\sqrt{gh} = 0.71$, was used for the numerical modeling of the flood).

Such feature is far from the results available in the literature, as many works are devoted to coastal events, such as tsunamis (e.g., Suppasri et al., 2013; Charvet et al., 2014; Petrone et al., 2017), i.e. singular unsteady shock events that do not properly represent typical urban floods. Such events are often studied through dam-break tests, collecting the hydrostatic and hydrodynamic forces acting on the building (Árnason, 2005; Cuomo et al., 2008; Nistor et al., 2010; Liang et al., 2016; Sarjamee et al., 2017).

However, tsunami-induced floods generate significant peak slamming forces on the structures (buildings, bridges, river banks, etc.), while the goal of the present study is to evaluate the action of a quasi-steady flow, which provides stresses, torques and buoyancy forces on buildings, similarly to what happens

with river-induced floods. Quasi-steady flow features also concern changes in the flow depth between upstream and downstream cross-sections (Fenton, 2003), generation of a hydraulic jump and standing waves, both downstream of the structure (Qi et al., 2014).

This process is similar to river flow around bridge piers, which is a long-time studied problem. So far, drag forces and coefficients have been analyzed for different flows and Reynolds numbers, as well as for different pier shapes (Lindsey, 1938; Roshko, 1955; Heddleson et al., 1957). Summary results on the drag coefficient are available in manuals and design specifications, which suggest large drag coefficients for square piers, such as $C_D = 1.4$ (AASHTO, 2013) or $C_D = 2$ (FEMA, 2011). However, design specifications are precautionary. More detailed works highlight the oscillating behavior of the drag forces, due to the vortex shedding and related to the Reynolds number (Almasri and Moqbel, 2017). The role of the incidence angle on square cylinders have been investigated, with focus on the vortex shedding, using air flow at low Reynolds numbers (e.g., see Dutta et al., 2008; Yoon et al., 2010). Numerical modeling have been used to study the fluid dynamics around bridge piers, this allowing the analysis of additional characteristics, such as local pressures on the pier walls (Wang et al., 2015; Nasim et al., 2018) or vortex shedding induced by complex geometries, like tandem piers (Almasri and Moqbel, 2017; Debus et al., 2003).

The present work evaluates the pressure field around a rectangular cylinder and the related hydrodynamics due to a quasi-steady flood with Reynolds numbers $Re = 10^5 \div 10^6$. Specifically, the influence of some important characteristics (depth, velocity, angle) of a flow impacting a building is studied, so as to construct a useful dataset to be exploited for both further experimental analyses and calibration/validation of numerical models aimed at reproducing the flow-structure interaction. To represent the construction type of interest, the model reproduces, at a reduced scale, a masonry building. The experimental tests were carried out in the flume of the Laboratory of Hydraulics and Maritime Constructions of the Università Politecnica delle Marche (Ancona, Italy). To quantify both hydrodynamics and loads on the building, water pressures have been measured at different locations on the building.

The paper is structured as follows. Section 2 describes the flume experiments, whose processed data are reported in section 3. Section 4 provides an overall discussion of the main results, while section 5 closes the paper.

2. Materials and Methods

In the following, the experimental tests carried out at the Università Politecnica delle Marche are described.

2.1. Flume experiments

The laboratory tests were carried out in a 50m-long, 1.3m-deep and 1m-wide channel, commonly used for coastal and offshore engineering purposes (Lorenzoni et al., 2010; Miozzi et al., 2015; Lorenzoni et al., 2016), due to a

115 wave paddle in the flume used for the generation of either regular or irregular waves. The channel (Figure 2a,b) is made of steel uprights and glass walls, while the bottom over which the tests were carried out is made of concrete mortar.

120 A free-from-obstacle length of about $16m$ was used for the present study. A mechanical system was built in the channel for the experiment at hand. Such system was made of an electrical engine which was connected to a trolley by means of four pulleys and a toothed belt (Figure 2a,b). The effect of the flow hitting the building has been obtained by moving the building in the water at rest, hence reproducing typical flood conditions by exploiting a non-inertial reference frame.

The boundary layer which develops from the interaction between water and plate in motion is small. In particular, low- and high-flow conditions (see test characteristics in the following) lead to the development of, respectively, laminar (Reynolds number $Re = 1.8 \times 10^5$) or turbulent ($Re = 6.0 \times 10^5$) boundary layers, whose thickness was of only few millimeters (Schlichting et al., 1974), with a reduced impact on the local hydrodynamics and almost null effects on the global hydrodynamics (see also section 4). Further, although the building might resemble a partially submerged vehicle (e.g., Arrighi et al., 2015), which experiences vertical/lifting forces, the present experiment is characterized by a rigid separation between the lower fluid region (under the plate) and the upper region (over the plate, where the building is located). Hence, the pressures measured at the four building walls are not affected by the hydrodynamics developing in the lower region. In addition, the non-inertial approach of the present work has already been used and validated by Haehnel and Daly (2002, 2004) to study the impact force of woody debris on structures.

140 The model reproduces, using a 1:10 scale, a bay of a building (Figure 2c). It was composed of a two-level structure, with basis of $0.31m$ by $0.25m$, of steel beams and pillars, where rigid floors were reproduced with a steel plate and the infill walls were built in masonry with bricks at a scale of 1:10 and concrete mortar. The use of such materials was aimed at properly mimicking the typical roughness of a masonry building and at reproducing a suitable hydrodynamics around the structure. However, laboratory experiments are typically carried out using materials different from those actually used in the real-scale prototype, mainly for the sake of convenience and simplicity. This leads to different surface/wall roughness, which can be defined using, e.g., Manning's parameter n (Chow, 1959). Some of the commonly used materials to reproduce impacts of water flows on civil engineering structures are: plastic ($n \approx 0.009s/m^{1/3}$, e.g. Azinfar and Kells, 2009), wood ($n \approx 0.017s/m^{1/3}$, e.g. Soares-Frazão and Zech, 2008), cast iron or aluminum ($n \approx 0.013s/m^{1/3}$, e.g. Ranga Raju et al., 1983; Cuomo et al., 2008). Under a physic and geometric viewpoint, use of bricks and mortar enables one to better mimic the actual roughness of a masonry building ($n \approx 0.025s/m^{1/3}$), also due to the impervious regions given by the brick-mortar alternation, which do not exist in "continuous" materials (e.g., aluminum). A suitable representation of the real-world roughness thus leads to a suitable representation of both wall boundary layer and pressure field around the structure.

160 The model did not reproduce an entire building, since the goal of the work
 was the analysis of the hydrodynamic effects induced by a specific construction
 type subject to flood. The structure was fixed to the trolley using a $0.155m$ -high
 plate, representing the bottom in the non-inertial reference frame, and a vertical
 pivot, that allowed for rotation of the building up to 360° . The trolley structure
 165 was composed by a thin plate supported by circular pillars (Figure 2b), which
 minimize the disturbance of the moving trolley on the fluid. Specifically, the
 geometry of plate, pillars and trolley have been designed to avoid undesirable
 effects on the flow field and to allow a suitable reproduction of a flood impacting
 a masonry building. To this aim, trolley and plate were characterized by a slight
 170 thickness and a significant length, which led to a reduced effect of the boundary
 layer at the building toe, and to completely and rigidly separate the building
 from the lower part, i.e. that between trolley and plate.

The masonry was equipped with six Piezoresistive Pressure Transmitters,
 Keller - Series 23SY, with pressure range: $(-200mbar, 200mbar)$. Two sensors
 175 were installed at each of the larger faces and one at each smaller face (Figure 2d
 illustrates a top view of the sensor mounting locations). They were all located
 $7.5cm$ above the basis of the structure (Figure 2c).

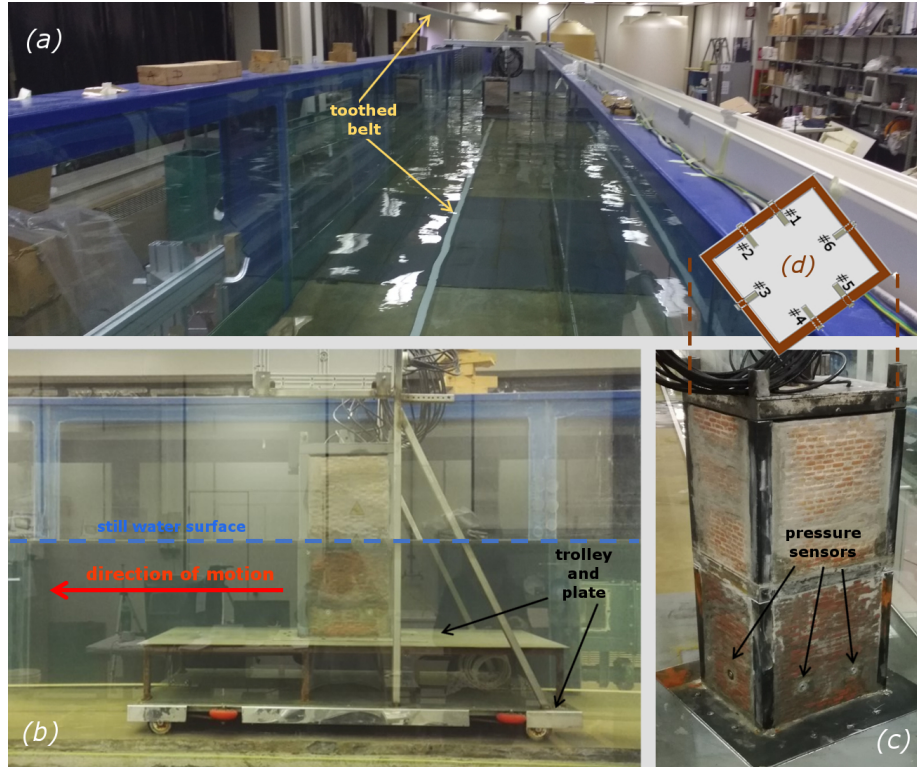


Figure 2: Building in the channel: (a) frontal/top view, (b) side view. (c) Detail of the masonry structure with pressure sensors, (d) top view of sensor location.

Each test was characterized by a series of phases, as described in the following. At the beginning, the building is at rest. Then, the building starts its motion and accelerate (order of $0.1s$), after which the velocity is kept constant (order of $10s$). The constant velocity was guaranteed by a power inverter connected to the engine and checked through use of both a tachometer and photocells. Finally, the building decelerates (order of $0.1s$) and stop.

The pressure sensors recorded at a frequency of $33Hz$ during each test. The data collected during the first (rest) phase has been used to evaluate the pressure in the static condition p_s . The data collected during the constant velocity phase are used to evaluate the overpressure in the dynamic condition.

Specifically, the raw data have been reduced of p_s , then a low-pass filter has been applied for the spike removal from the signal and the overpressure in dynamic condition p_d has been obtained by averaging over a $3s$ interval in the central part of the constant-velocity phase. Such small time range is chosen to omit acceleration/deceleration phenomena. The total pressure in the dynamic condition p_t has been gotten by summing up the above contributions.

During the experimental campaign, three flow characteristics were varied: the angle θ , representing the incidence of the flow on the building; the building velocity v , representing the flow velocity; and the water depth h . Five angles ($\theta = 0^\circ, 22.5^\circ, 45^\circ, 67.5^\circ, 90^\circ$), six velocities ($v = 0.326m/s, 0.465m/s, 0.605m/s, 0.744m/s, 0.884m/s, 1.023m/s$) and four water depths ($h = 0.095m, 0.145m, 0.195m, 0.245m$) were used, for a total of 120 test configurations. Each of these configurations was repeated four times to check test repeatability.

Water depth h and velocity v are combined using the dimensionless Froude number $Fr = v/\sqrt{gh}$, with g the gravity acceleration. The generic pressure p is made dimensionless as follows: $\tilde{p} = p/\rho v^2$, with ρ the water density.

Values of Fr much larger than 1 have not been tested. Specifically, due to limitations of the used mechanical system (e.g., the engine power), velocities larger than $1.023m/s$ could not be reproduced in such physical model. Further, depths smaller than $0.095m$ have not been analyzed, as frictional effects could significantly affect the results (e.g., see Qi et al., 2014). However, although highly supercritical conditions, like those characterizing flash floods (Diakakis et al., 2019), are not accounted for, the Fr range is wide (see section 2.2), also compared to recent researches where $Fr \ll 1$ (e.g., Qi et al., 2014).

2.2. Analysis of experimental data

During the constant velocity phase, the fluid free surface changes its shape: a super-elevation occurs upstream and a level reduction downstream of the building. Figure 3 illustrates, for different incidence angles, the two limit cases which have been analyzed: the maximum Froude-number case (i.e. $Fr = 1.060$, given by $v = 1.023m/s$ and $h = 0.095m$) and the minimum Froude-number case (i.e. $Fr = 0.210$, given by $v = 0.326m/s$ and $h = 0.245m$), reported in the left and right panel, respectively. Hereafter, the two limit cases will be referred as “Fmax” and “Fmin”. The variation of the free surface in the two cases is significantly different: in the “Fmin” case, a slight surface variation

occurs, mainly at the downstream side of the building, probably related to the wake (left panels of Figure 3); in the “Fmax” case, the change in water depth is larger and the flow is characterized by a stationary wave upstream and by an hydraulic jump downstream (right panels of Figure 3). Such conditions are also shown and modeled by Qi et al. (2014).

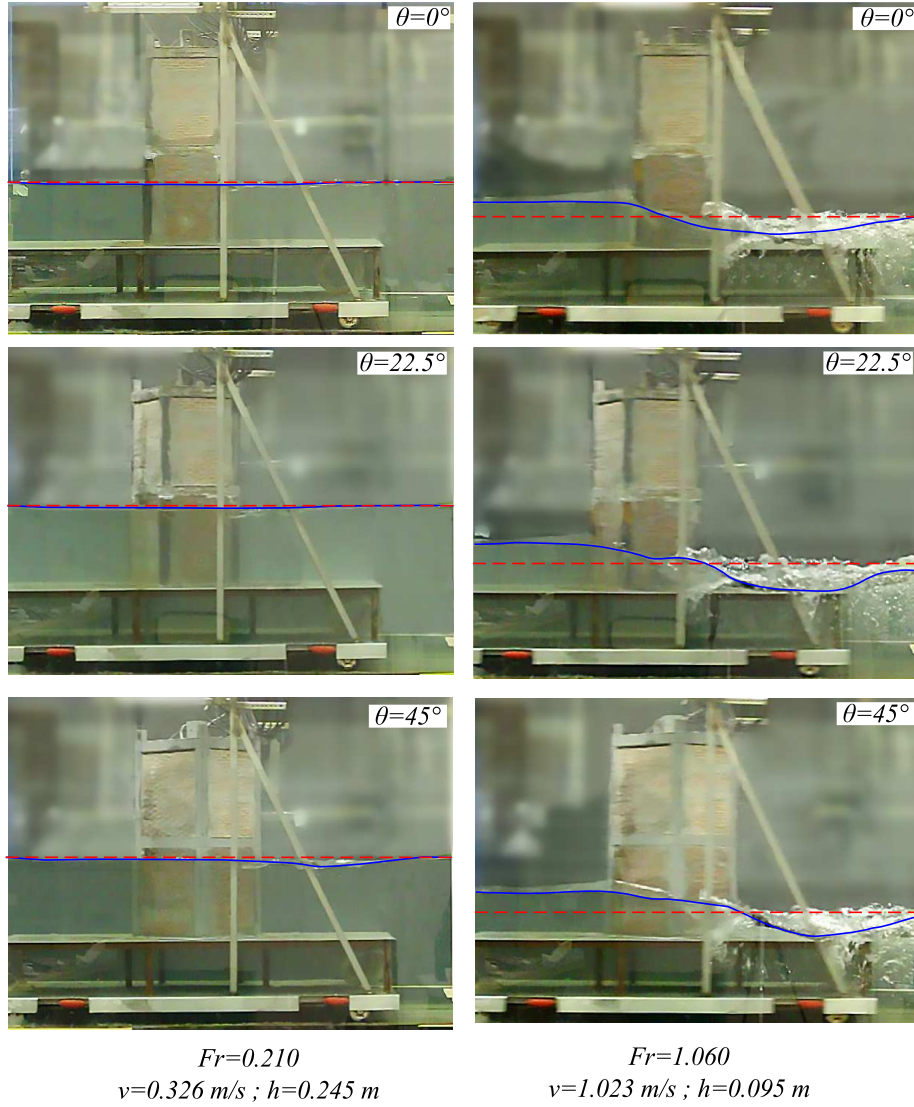


Figure 3: Snapshots of some experimental tests, showing the still water surface (red dashed lines) and instantaneous surface (blue lines). Two limit conditions are illustrated: “Fmin” (left column) and “Fmax” (right column) for some of the tested incidence angles: $\theta = 0^\circ$ (top row), $\theta = 22.5^\circ$ (middle row) and $\theta = 45^\circ$ (bottom row).

The results obtained from the data collected by the six pressure sensors, i.e. the pressure in the static condition p_s and the overpressure in the dynamic condition p_d , have been analyzed with the aim to estimate the hydrodynamics around the structure during the different tested conditions. Though p_d has been evaluated in the constant velocity phase, it was characterized by an oscillating evolution (see Figure 4 and 5), **which is due to the vortex shedding**.

2.2.1. Overpressure in dynamic condition

As significant example conditions, the overpressure p_d derived for “Fmax” and “Fmin” cases, with null incidence between flow and structure, is analyzed.

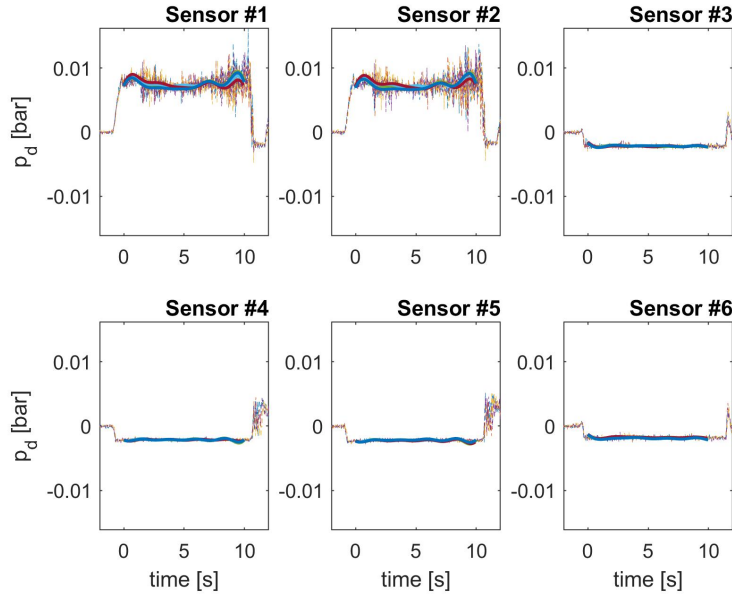


Figure 4: Time series of the overpressure in the dynamic condition p_d measured by each sensor during the “Fmax” tests with $\theta = 0^\circ$. Raw data (dashed thin lines) and filtered data (solid thick lines).

Figure 4 illustrates the time series recorded by each sensor during the four tests of the “Fmax” case, reduced by the pressure evaluated during static conditions p_s . Notice that the raw data (dashed thin lines) span between an initial rest/flat phase (with pressure essentially null), followed by a sudden acceleration, and an almost constant velocity region and a rapid deceleration. Filtering is only applied to the almost constant velocity region (solid thick lines), i.e. that used for the calculation of p_d . To graphically compare the four tests, each signal has been properly shifted back, with the time $t = 0$ referring to the beginning of the filtered series.

Sensors 1 and 2, in the present configuration representing those at the frontal surface, provide the largest overpressure in dynamic condition, while both lat-

250 eral (sensors 3 and 6) and rear (sensors 4 and 5) overpressures are negative. Such negative overpressures are an order of magnitude smaller than those characterizing the impact surface, i.e. $O(10^{-2})\text{bar}$ vs $O(10^{-3})\text{bar}$. Besides, only slight oscillations occur during the almost constant phase for each test at each sensor. In addition, both raw and filtered data are significantly similar in the four tests, thus demonstrating test repeatability.

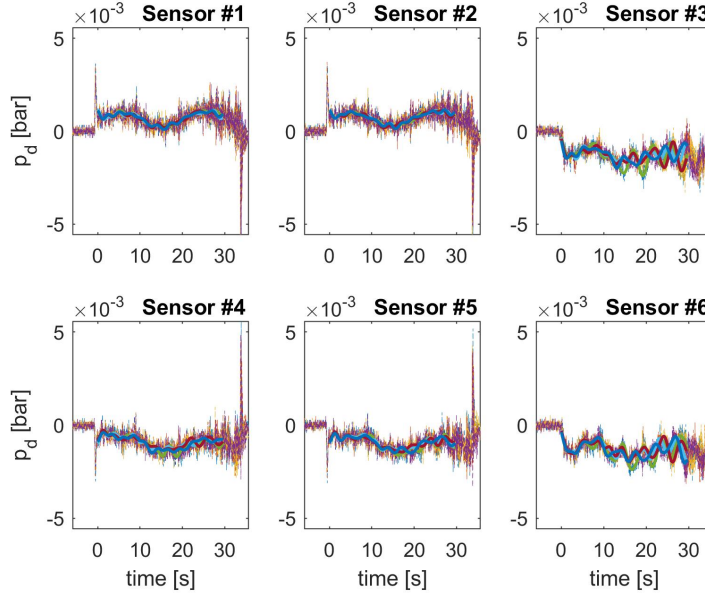


Figure 5: Time series of the overpressure in the dynamic condition p_d measured by each sensor during the “Fmin” tests with $\theta = 0^\circ$. Raw data (dashed thin lines) and filtered data (solid thick lines).

255 On the other hand, Figure 5 represents the time series for the tests of the “Fmin” case, with null incidence, reduced by the pressure evaluated during static conditions p_s . Oscillations during the almost constant velocity phase are now much more evident than in the previous case, with the lateral sensors providing more frequent variations. Such behavior is detectable even when the same axis limits are used for Figures 4 and 5. Also in this case, frontal sensors provide positive overpressures in dynamic conditions, while both lateral and rear overpressures are negative. The order of magnitude is the same at each structure wall, i.e. $O(10^{-3})$.

265 Due to the small duration of the constant velocity phase of each test ($\approx 30\text{s}$ for Fmin and $\approx 10\text{s}$ for Fmax), numerical simulations have been run using the commercial code ANSYS Fluent. For the Fmax case (experimental data in Fig. 4), the numerical results obtained the same experimental non-inertial approach, i.e. a rigid body moving along a straight rectangular channel with water at rest, properly reproduce the experimental data at each sensor location.

270 With the aim to check if a quasi steady-state condition is reached after few seconds, the time evolution of the hydrodynamic force acting at the frontal wall has been estimated from the numerical simulation. In detail, just 3s after the initial motion of the rigid body, the force value is very close to the asymptotic value reached after a simulation time of 8s, with maximum errors $\approx 5\%$. Hence, the overpressure p_d calculated during the constant velocity phase refer to a quasi-steady condition.

275 Details of such topic will be given in a future work, devoted to numerical simulations of flood-building interaction.

2.2.2. Power spectral density

280 With the aim to investigate the role of oscillations produced by the structure during its run, a spectral analysis has been performed. In particular, the power spectral density (PSD) of the “Fmax” case is shown in Figure 6, while the PSD of the “Fmin” case is illustrated in Figure 7.

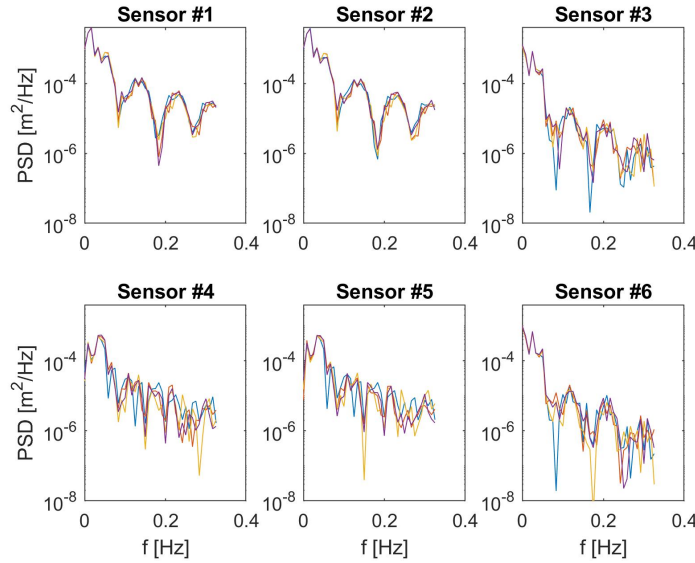


Figure 6: PSD of the overpressure in the dynamic condition p_d characterizing the “Fmax” case ($h = 9.5cm$, $v = 1.023m/s$ and $\theta = 0^\circ$).

285 The spectral densities referring to the different tests overlap fairly well for each sensor, especially for the frontal ones and at larger velocities (see sensors 1 and 2 in Figure 6). Further, the peak frequencies f_p are almost exactly the same. Specifically, the “Fmax” case (Figure 6) provides a peak frequency at the frontal sensors $f_{p,12} = 0.017Hz$, which corresponds to a peak period $T_{p,12} = 1/f_{p,12} \approx 60s$, while the lateral and rear sensors are characterized, respectively by peak frequencies $f_{p,36} = 0.025Hz$ and $f_{p,45} = 0.033Hz$, and peak periods $T_{p,36} = 1/f_{p,36} \approx 40s$ and $T_{p,45} = 1/f_{p,45} \approx 30s$. The “Fmin”

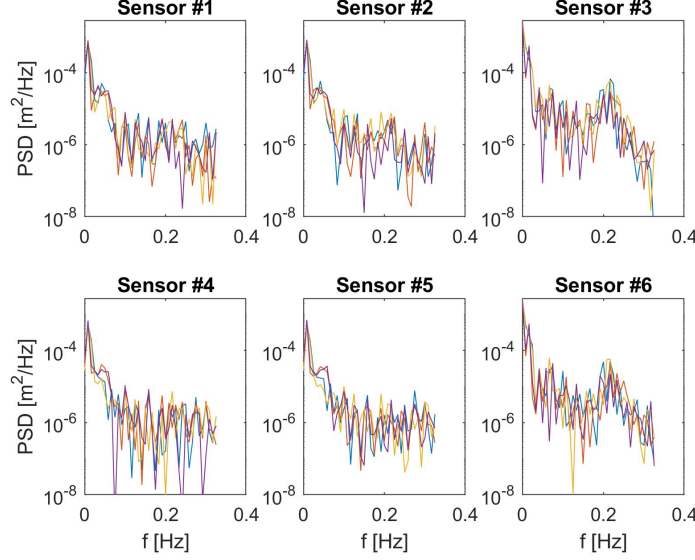


Figure 7: PSD of the overpressure in the dynamic condition p_d characterizing the “Fmin” case ($h = 24.5\text{cm}$, $v = 0.326\text{m/s}$ and $\theta = 0^\circ$).

case (Figure 7) provides $f_{p,12} = f_{p,45} = 0.008\text{Hz}$ and $T_{p,12} = T_{p,45} \approx 120\text{s}$ at both frontal and rear sensors, while the lateral sensors are characterized by $f_{p,36} = 0.017\text{Hz}$ and $T_{p,36} \approx 60\text{s}$.

3. Processing the overpressure in dynamic conditions

A comparison among the different configurations is provided in the following sections. In particular, the overpressure in the dynamic condition p_d at the surfaces of the building is presented by inspecting the influence of the different parameters varied during the experiments. The large amount of combinations among the involved parameters hinders an immediate analysis including all such parameters. Hence, the dependence of p_d on each single parameter is first analyzed, then the influence of all variables is investigated.

3.1. Overpressure and velocity

The variation of p_d with velocity is evaluated at the sensor locations fixing the water depth and the incidence angle.

Figure 8 reports such information for the two edge cases, i.e. those characterized by $h = 9.5\text{cm}$ and $h = 24.5\text{cm}$. The largest velocity produces the largest overpressure p_d at the impact surface, as expected. Conversely, small velocities provide a reduced pressure increase at the frontal sensors. Quantitatively, looking at the top panel of Figure 8, while the case with $v = 0.326\text{m/s}$ is characterized by $p_d = 32\text{Pa}$, the case with $v = 1.023\text{m/s}$ provides $p_d = 702\text{Pa}$.

Hence, with significantly small water depths ($h = 9.5\text{cm}$) and flow perpendicular to the building ($\theta = 0^\circ$), an increase of a factor 3 in the velocity magnitude provides an increase in the overpressure p_d , which is more than 20 times larger.

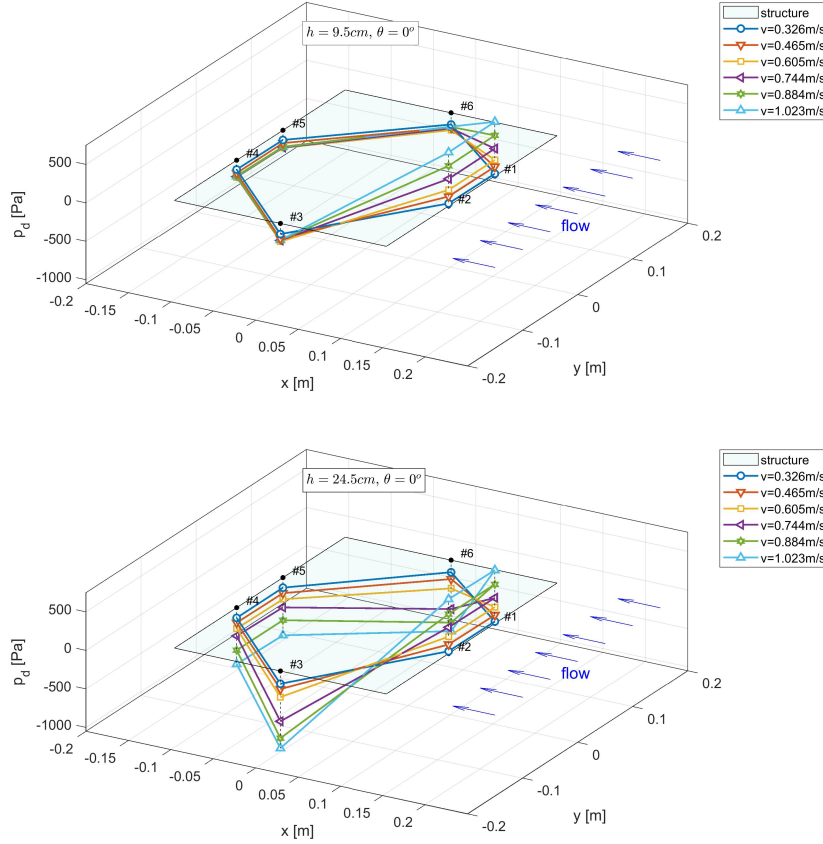


Figure 8: Overpressure p_d measured by each sensor during tests with $h = 9.5\text{cm}$ and $\theta = 0^\circ$ (top) and $h = 24.5\text{cm}$ and $\theta = 0^\circ$ (bottom). Note that symbols provide p_d values, while lines simply connect such points.

A similar behavior exists when the water depth is larger (Figure 8, bottom panel). The cases characterized by $h = 24.5\text{cm}$ and $\theta = 0^\circ$ shows a similar increase of p_d with the velocity rise, providing $p_d = 28\text{Pa}$ and $p_d = 699\text{Pa}$ with the smallest and largest tested velocities, respectively. The same considerations can be made for the other tested depths, hence all tested depths with null incidence flow provide a significant p_d increase (factor between 20 and 25) as a consequence of a small velocity increase (factor 3).

Both lateral and rear surfaces experience negative dynamic pressures, but the order of magnitude is the same for all tested velocities, with p_d varying in the

range $[-220, -120]Pa$. While larger depths provide clear trends, i.e. p_d decrease with velocity (bottom panel), smaller depths do not reveal a clear trend, with p_d slightly changing (increasing or decreasing) with velocity. Hence, a small depth (e.g., $h = 9.5cm$) promotes a reduced or null p_d decrease, which means a reduced or null water level decrease, this behavior suggesting the existence of a velocity-depth threshold on p_d . Such threshold depends on the weight of the bottom boundary layer within the water column. Its thickness is a function of $Re_x = vx/\nu$ (Schlichting et al., 1974), i.e. of the flow velocity affecting the building v , the distance along the plate x and the kinematic viscosity ν . The layer thickness is of the order of millimeters and is expected to affect the hydrodynamics along the depth h . Hence the existence of a threshold depending on the $h-v$ pair. Although such differences in the local hydrodynamics, the global hydrodynamics are essentially close to those found using a traditional inertial approach (see section 2.1).

To summarize, the influence of the flow velocity on the overpressure is large at the upstream face of the building, and suggests the existence of a threshold at the lateral and rear faces of the building.

3.2. Overpressure and initial water depth

Similarly to what presented in the previous section, the variation of p_d with the initial water depth h is shown, fixing the velocity and the incidence angle. Figure 9 illustrates the results of the tests characterized by $v = 0.326m/s$ and $v = 1.023m/s$. The water depth seems to only slightly change the overpressure in the dynamic condition. As already observed, the largest velocity produces the largest overpressure at the impact surface: the smallest velocity (top panel of Figure 9) provides $p_d \approx 30Pa$, while the largest velocity (bottom panel of Figure 9) provides $p_d \approx 700Pa$. Such overpressures are independent of h .

Concerning the test with $v = 0.326m/s$ (top panel), the overpressure at the lateral surfaces ranges in $p_d \approx [-180, -140]Pa$, while it is $p_d \approx [-150, -120]Pa$ at the rear surface. Conversely, tests with $v = 1.023m/s$ (bottom panel) are characterized by a lateral overpressure significantly dependent on the water depth, with a decrease from $p_d \approx -180Pa$ (for $h = 9.5cm$) to $p_d \approx -1000Pa$ (for $h = 24.5cm$). Similarly, the rear overpressure decreases from $p_d \approx -210Pa$ (for $h = 9.5cm$) to $p_d \approx -750Pa$ (for $h = 24.5cm$).

Hence, the overpressure is independent of the initial water depth h at the frontal surface, while it is significantly influenced by h laterally and downstream. This occurs for large velocities, while small flow velocities suggest a weak dependence of p_d on h at the lateral and rear walls.

3.3. Overpressure and incidence angle

The variation of the dynamic pressure is here analyzed as a function of the flow incidence on the structure. As in the previous analyses, p_d is studied fixing the initial water depth h and the velocity v , and varying the incidence angle θ . Figure 10 illustrates the results of the tests characterized by “Fmin” (top panel) and “Fmax” (bottom panel), respectively. A significant variation of the

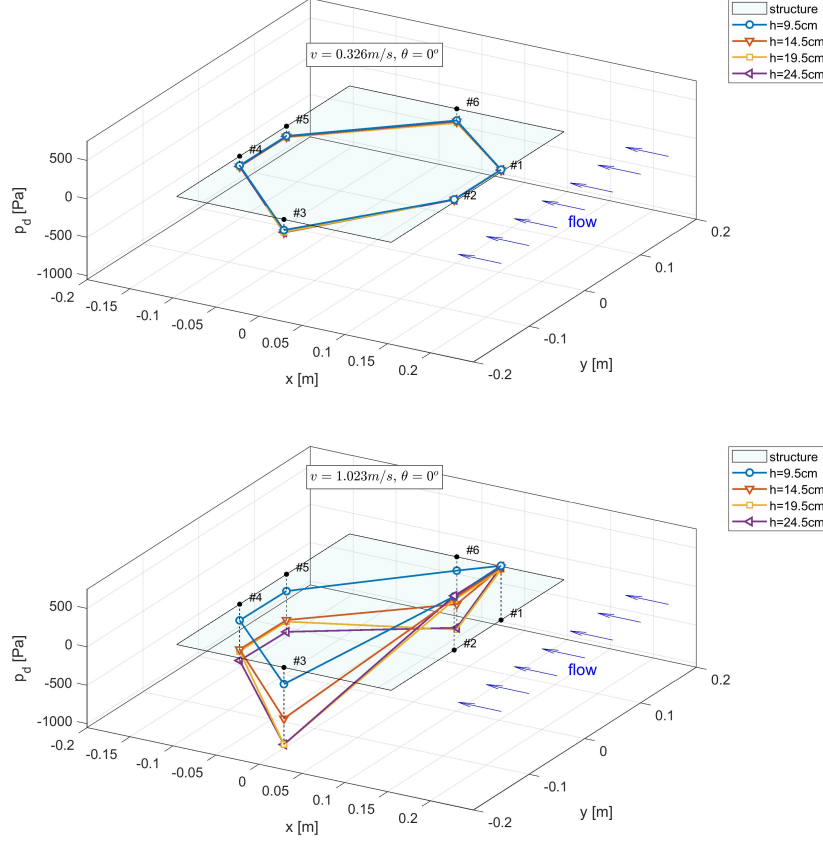


Figure 9: Overpressure p_d measured by each sensor during tests with $v = 0.326\text{m/s}$ and $\theta = 0^\circ$ (top) and $v = 1.023\text{m/s}$ and $\theta = 0^\circ$ (bottom). Note that symbols provide p_d values, while lines simply connect such points.

overpressure affects sensors 1, 2 and 6, in terms of both sign and modulus, since they are the only sensors to pass from the frontal wall (hence measuring positive overpressures) to a lateral wall (hence measuring negative overpressures) or vice versa.

For the “Fmin” case, at sensor 1, p_d varies from a minimum value $\cong -180\text{Pa}$ ($\theta = 90^\circ$) to a maximum value $\cong 40\text{Pa}$ ($\theta = 22.5^\circ$). At sensor 2, p_d changes from $\cong -150\text{Pa}$ ($\theta = 90^\circ$) to $\cong 30\text{Pa}$ ($\theta = 0^\circ$), while sensor 6 changes from $\cong -170\text{Pa}$ ($\theta = 0^\circ$) to $\cong 30\text{Pa}$ ($\theta = 90^\circ$). Hence, the 90° flow rotation leads to an exchange of overpressure values on the building walls, with an almost complementary behavior, i.e. there is always a wall characterized by a significantly large negative overpressure, $p_d \approx [-180, -150]\text{Pa}$, and another wall subject to a significantly small positive overpressure, $p_d \approx [30, 40]\text{Pa}$.

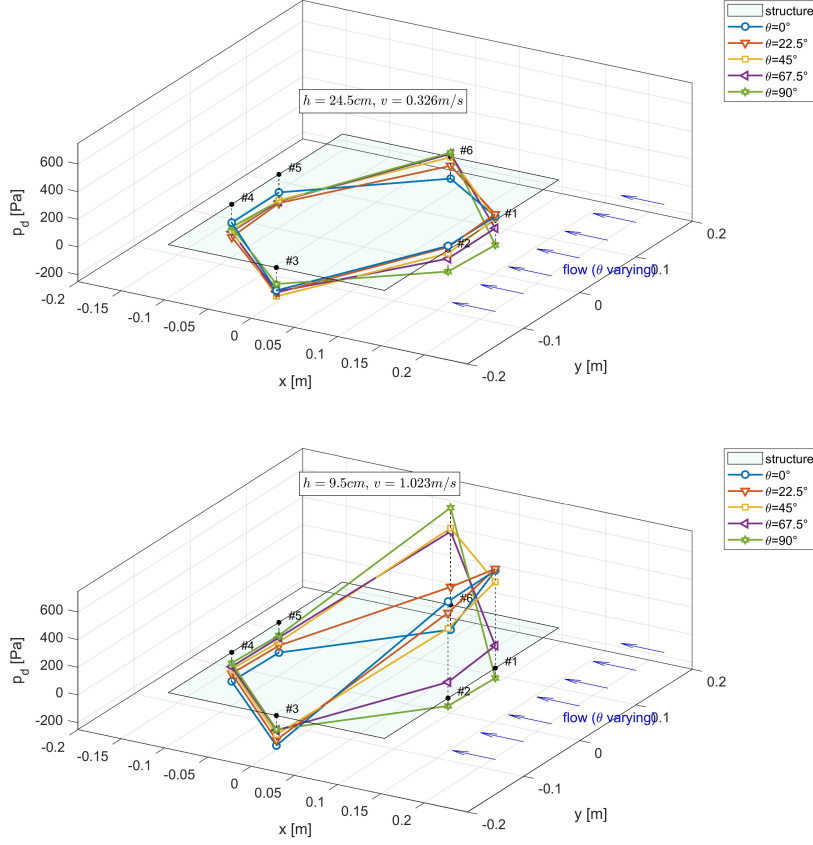


Figure 10: Overpressure p_d measured by each sensor during tests “Fmin” ($v = 0.326\text{m/s}$ and $h = 24.5\text{cm}$, top) and “Fmax” ($v = 1.023\text{m/s}$ and $h = 9.5\text{cm}$, bottom). Note that symbols provide p_d values, while lines simply connect such points.

The overpressure difference between sensors 1 and 2 (respectively located more upstream and downstream for $\theta > 0^\circ$) changes with the flow angle. In particular, if $p_{d,1}$ and $p_{d,2}$ define the overpressures at the two sensors, the 45° case provides the largest overpressure gradient among the tested angles, with $p_{d,2} - p_{d,1} = -36\text{Pa}$. Further significant differences may be observed for the 22.5° and 67.5° cases, where $p_{d,2} - p_{d,1} = -21\text{Pa}$ and -2Pa , respectively. This highlights how the flow incidence affects the overpressure distribution on the hit walls and, consequently, the overall hydrodynamics.

In the “Fmax” case, things are slightly different. In particular, while for $\theta = 0^\circ$ the overpressure $p_d \approx 700\text{Pa}$ at sensors 1-2 and $p_d \approx -180\text{Pa}$ at sensor 6, for $\theta = 90^\circ$ the overpressure $p_d \approx [-60, -70]\text{Pa}$ at sensors 1-2 and $p_d \approx 700\text{Pa}$ at sensor 6. Hence, the large positive pressure at the impact wall is

always of the same order ($\approx 700Pa$), while the negative pressure at the lateral wall changes significantly (-60 to $-180Pa$). Such a behavior is probably due to the blocking effect, which mainly acts on the lateral walls (see section 3.4).

As discussed for the “Fmin” case, the overpressure measured by sensors 1 and 2 during “Fmax” provides the following results. The largest overpressure gradient and water-level change occur for $\theta = 45^\circ$, where $p_{d,2} - p_{d,1} = -119Pa$, while such difference is $-101Pa$ and $-46Pa$ for, respectively, $\theta = 22.5^\circ$ and 67.5° . This confirms the dependence of the overpressure distribution on the flow angle and highlights a steeper water surface during high-flow conditions, hence a significant change in the free-surface geometry.

In both cases, the overpressure p_d at sensors 3, 4 and 5 is always negative, while the modulus does not change significantly, as such sensors are never directly impacted by the flow and are always measuring negative overpressures.

Hence, the tested cases show that a significant variation of the overpressure occurs when the flow approaches the building with an angle, with different behaviors in the case of small and large Froude numbers. Such differences depend on the blocking effect, but also on the water momentum flux. Analytical laws confirm an increase of the backwater profile with an increasing Fr value (e.g., Chow, 1959).

Tests characterized by further Fr values have not been included here for the sake of brevity. However, synthetic results coming from the whole data set are illustrated in the following sections.

3.4. Overpressure and blocking effect

The blocking effect depends on the ratio between the structure width b and the channel width w , as analyzed in the recent literature (e.g., Fenton, 2003; Qi et al., 2014). It is thus important to analyze the conditions during which the flow perpendicularly impacts a rectangular cylinder, i.e. the experimental tests characterized by $\theta = 0^\circ$ (sensors 1 and 2 are at the impact surface) and $\theta = 90^\circ$ (sensors 6 is at the impact surface). Figure 11 illustrates the results of the tests characterized by the minimum (top panel) and maximum (bottom panel) velocity and depth. The cases with $\theta = 0^\circ$ (in red) and $\theta = 90^\circ$ (in green) refer to, respectively, a blocking ratio $b/w = 0.25$ and $b/w = 0.31$.

The order of magnitude of p_d at the different surfaces is the same during both incidence conditions. The top panel shows a dynamic pressure $p_d = 35Pa$ and $29Pa$ at the impact surface, respectively when $\theta = 0^\circ$ and 90° . The bottom panel provides, respectively, $p_d = 699Pa$ and $649Pa$. Hence, though the different hydrodynamic conditions (h and v), the blocking effect seems to affect the water level upstream of the structure, in agreement with the b/w parameter. At the rear surface, $p_d = -123Pa$ and $-114Pa$ for the case with minimum velocity and depth (top panel of Figure 11), while $p_d = -741Pa$ and $-782Pa$ for the case with maximum velocity and depth (bottom panel of Figure 11), respectively when $\theta = 0^\circ$ and 90° . From the analysis of the pressure variation between the upstream and downstream cross sections ($\Delta p_d = p_d|_{up} - p_d|_{down}$), it results that the blocking effect induces a reduction of less than 10% when b/w

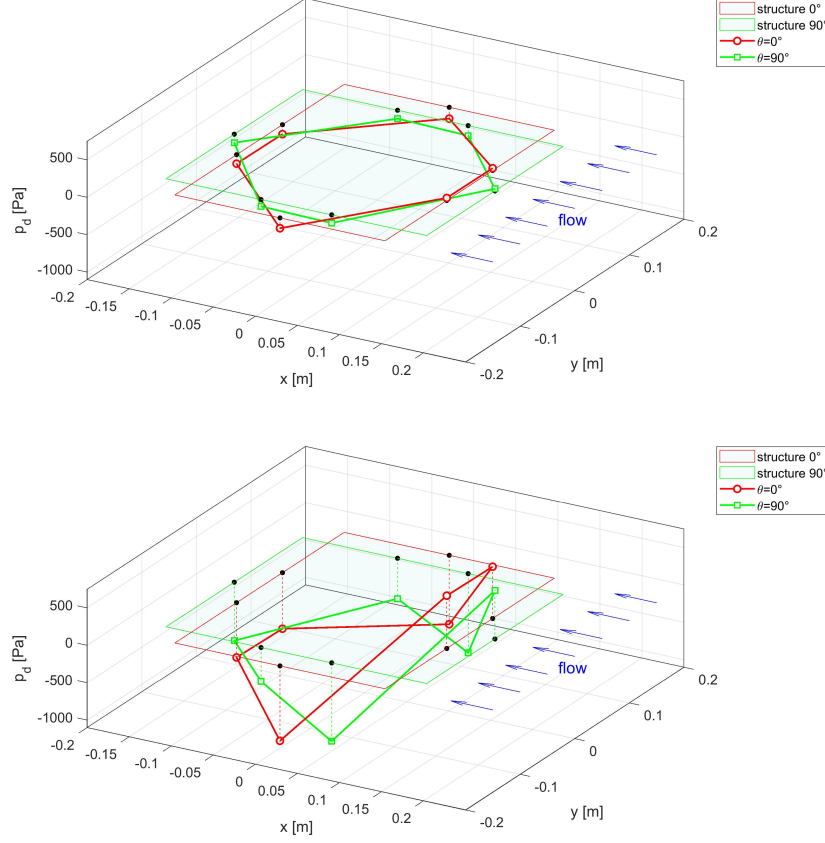


Figure 11: Overpressure p_d measured by each sensor during tests with $h = 9.5\text{cm}$ and $v = 0.326\text{m/s}$ (top) and $h = 24.5\text{cm}$ and $v = 1.023\text{m/s}$ (bottom). Note that symbols provide p_d values, while lines simply connect such points.

changes from 0.31 to 0.25, i.e. when the flow incidence changes from 0° to 90° . The exact reduction rate strictly depends on the considered flow conditions h and v .

3.5. Power spectral density

The spectral analysis confirms the dependence of the overpressure on the variables reported in the previous sections. Specifically, the comparison between the PSD of the signal measured by each sensor during different velocity conditions (Figures 12 and 13) shows that, at each location, the largest power has been recorded during high-flow conditions ($v = 1.023\text{m/s}$, light blue line), while the smallest power has been recorded during low-flow conditions ($v = 0.326\text{m/s}$, dark blue line). Further, while the mean PSD is of order $10^{-4}\text{m}^2/\text{Hz}$ when the velocity is high ($v = 1.023\text{m/s}$), lower velocities ($v < 0.5\text{m/s}$) provide the

largest PSD at lower frequencies and a mean PSD of order $10^{-6}m^2/Hz$ (e.g., PSD at $f \approx 0.01Hz$ is much larger than PSD at higher frequencies). This occurs independently of h (see both Figures 12 and 13).

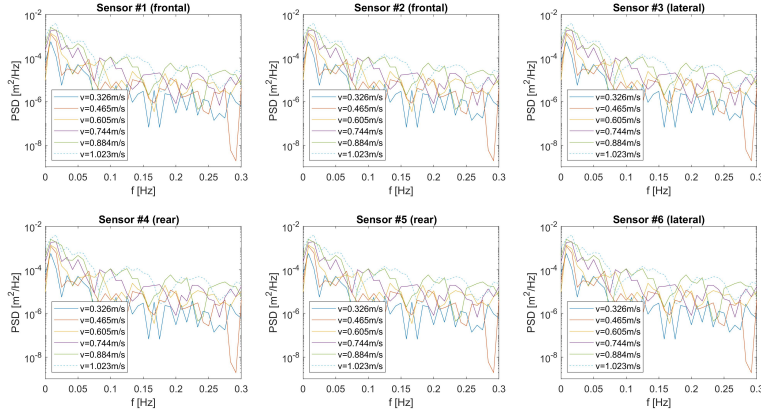


Figure 12: PSD of the overpressure p_d for tests with $h = 9.5cm$ and $\theta = 0^\circ$.

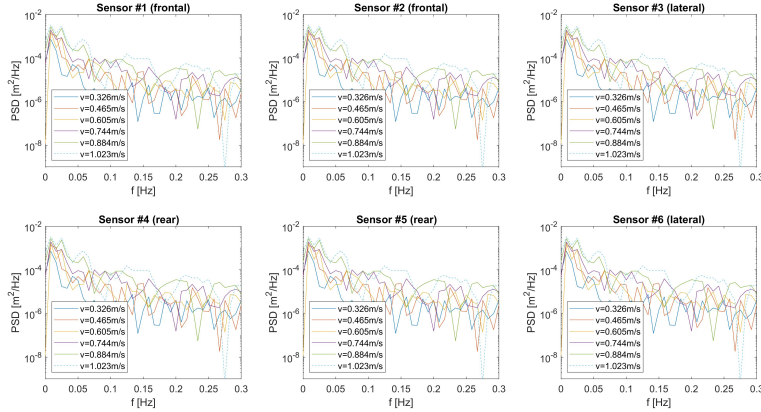


Figure 13: PSD of the overpressure p_d for tests with $h = 24.5cm$ and $\theta = 0^\circ$.

The spectral analysis further confirms the reduced dependence of overpressure on the initial water level h . In fact, for small velocities (Figure 14), similar patterns have been found at each sensor, with mean PSD of order $10^{-6}m^2/Hz$, while for large velocities (Figure 15) the curves overlap and are characterized by a PSD order of $10^{-4}m^2/Hz$.

When the flow angle is larger than 0° , things slowly evolves. Specifically, if $\theta \leq 45^\circ$, PSD patterns of all studied angles overlap pretty well, hence providing

455 the same peak frequencies, independently of the flow incidence. For $\theta = 67.5^\circ$, a transition occurs, i.e. low-frequency ($f < 0.08\text{Hz}$) PSD values are smaller than those observed for smaller angles. For $\theta = 90^\circ$, PSD values are significantly smaller than those observed for $\theta \leq 45^\circ$, this occurring throughout the frequency domain, where the PSD pattern is also completely different. Hence, a significant
 460 frequency redistribution can be observed when the flow incidence is $\theta > 45^\circ$.

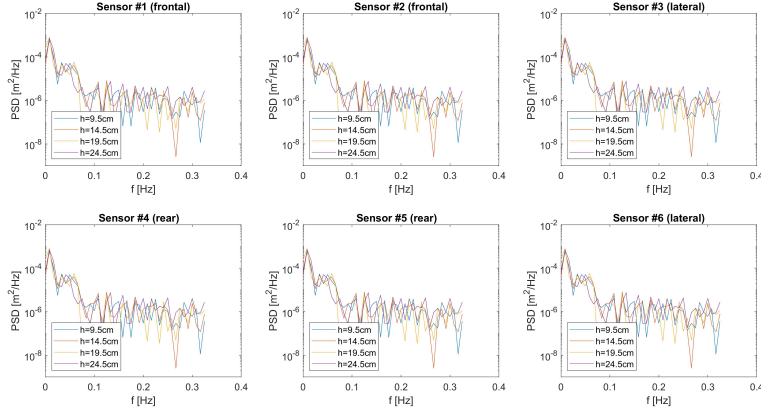


Figure 14: PSD of the overpressure p_d for tests with $v = 0.326\text{m/s}$ and $\theta = 0^\circ$.

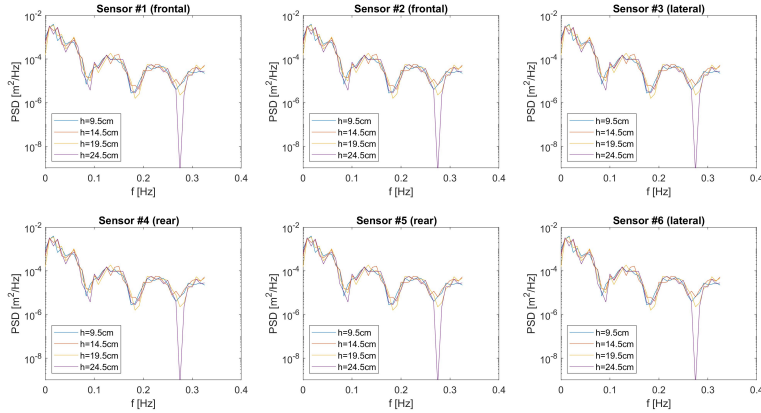


Figure 15: PSD of the overpressure p_d for tests with $v = 1.023\text{m/s}$ and $\theta = 0^\circ$.

3.6. Overpressure and flow characteristics

To better investigate the dependence of p_d on all tested flow characteristics, the dependence on the water flux hv^2 is first analyzed, such term being a combination of the tested velocities and initial water depths. This is inspired by the

465 expression of the drag force:

$$F_D = \frac{1}{2}\rho C_D h v^2, \quad (1)$$

where ρ is the water density and C_D the drag coefficient.

Figure 16 illustrates the overpressure in the dynamic condition, measured by each sensor during each configuration characterized by $\theta = 0^\circ$ (top panel), $\theta = 45^\circ$ (middle panel) and $\theta = 90^\circ$ (bottom panel), plotted versus the water
470 flux $h v^2$.

In the first case ($\theta = 0^\circ$), the measurements of the frontal sensors almost perfectly overlap (blue symbols), providing an almost linear positive evolution with the flux $h v^2$. An almost linear negative trend is observed for both rear (green symbols) and lateral (red symbols) measurements. All linear interpolations provide a fairly good best fit ($R^2 > 0.65$).
475

Similar behaviors are observed when $\theta = 90^\circ$ (bottom panel), where sensors 1, 2, 4 and 5 are lateral (red), while sensor 6 is frontal (blue) and 3 is rear (green). In this case, R^2 is good for all sensors, except for those located at the downstream lateral position, i.e. 2 and 4. This may be explained with the
480 tendency to reach an almost constant p_d for large flux values $h v^2$, partly due to an increased turbulence which characterizes nearly critical conditions and choked flows (Qi et al., 2014). Such a trend may be clearly observed in the distribution of the data collected by the frontal and lateral sensors.

The middle case, i.e. that characterized by $\theta = 45^\circ$, presents significantly
485 better trends if compared to the 90° case, as all fitting curves provide $R^2 > 0.5$, despite the angled flow incidence.

To better analyze the effect of the flow incidence on the overpressure p_d , Figure 17 illustrates the dependence of p_d on the water flux $h v^2$ for the three sensors characterized by the largest changes, i.e. sensor 1 (top panel), sensor 2
490 (middle panel) and sensor 6 (bottom panel), for each tested angle. In particular, the linear trend seems to properly fit the measured data, with $R^2 > 0.6$ when the sensors are frontal or rear. Conversely, the lateral overpressure is not always well represented by the linear trend. In particular, when p_d is small (hence the local surface level is small), this oscillates around zero. This happens at sensors
495 1 and 2, when $\theta = 67.5^\circ$, and at sensor 6, when $\theta = 22.5^\circ$. In such cases, the overpressure and water super-elevation significantly vary with the flux.

The dependence of p_d on the flow characteristics may also be detected in Figures 18 ($\theta = 0^\circ$), 19 ($\theta = 45^\circ$) and 20 ($\theta = 90^\circ$). As already observed in the previous sections, the frontal wall overpressure (sensors 1 and 2 in Figure 18,
500 sensor 1 in Figure 19, sensor 6 in Figure 20) is only slightly affected by the initial water depth and significantly affected by the flow velocity, with p_d varying between $30Pa$ and $700Pa$ when passing from $v = 0.326m/s$ to $v = 1.023m/s$. Conversely, h and v affect in a similar way the overpressure p_d measured at the lateral surfaces (sensors 3 and 6 in Figure 18, sensors 1 and 5 in Figure 20).

505 Notice that p_d at the most downstream lateral location (sensors 2 and 4 in Figure 20) is much smaller than p_d measured at the most upstream lateral location (sensors 1 and 5) and at the rear surface (sensor 3). This suggests that,

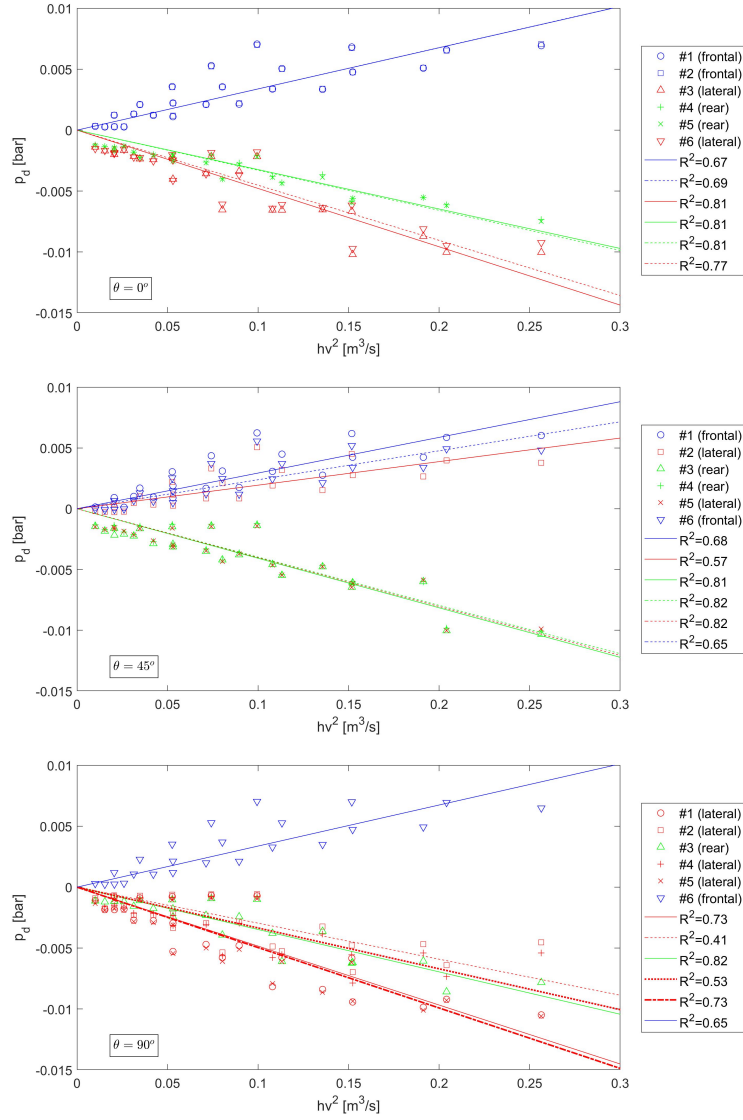


Figure 16: Overpressure p_d versus flux hv^2 for incidence angles $\theta = 0^\circ$ (top panel), $\theta = 45^\circ$ (middle panel) and $\theta = 90^\circ$ (bottom panel). Symbols provide p_d values and lines provide linear fitting.

after a water level increase at the frontal wall (sensor 6), this suddenly decreases at the lateral surfaces (sensors 1 and 5), then increases (sensors 2 and 4), finally it decreases again at the rear wall (sensor 3).

510

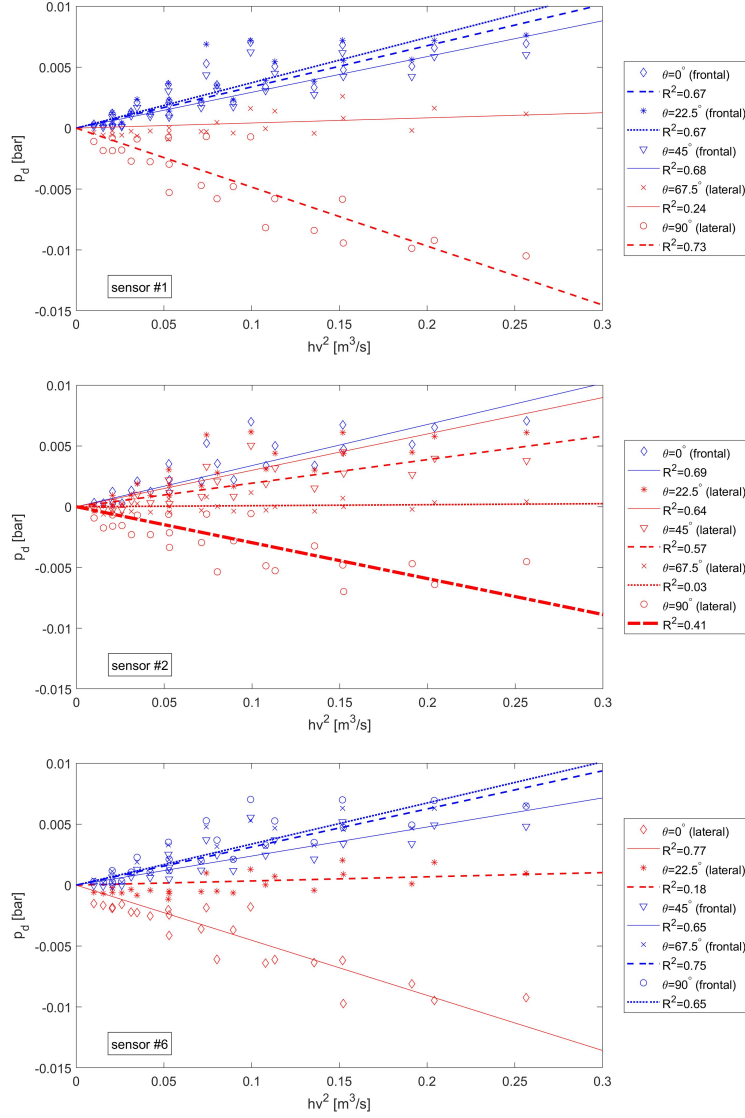


Figure 17: Overpressure p_d versus flux hv^2 for all incidence angles, measured at sensor 1 (top panel), sensor 2 (middle panel) and sensor 6 (bottom panel). Note that symbols provide p_d values and lines provide linear fitting.

4. Discussion

The results obtained for the overpressure p_d (e.g. those reported in Figures 8, 9 and 10) can be extended to the water super-elevation η generated during the tests, i.e. $\eta = p_d/(\rho g)$. In particular, the positive value of p_d at the frontal

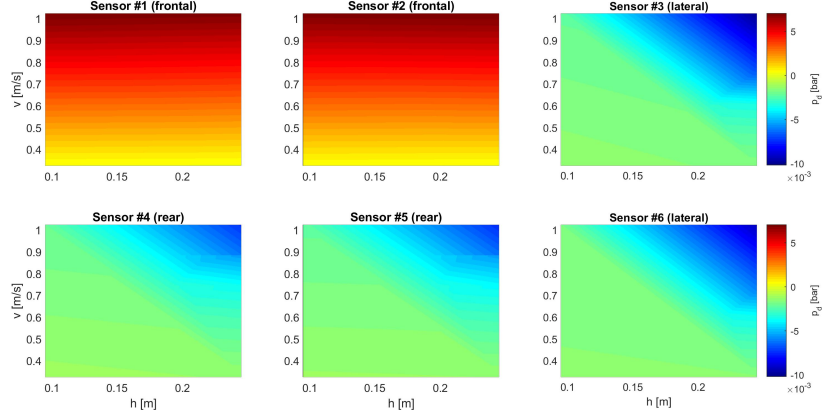


Figure 18: Overpressure p_d at each sensor as a function of the flow characteristics h and v . Flow incidence: $\theta = 0^\circ$.

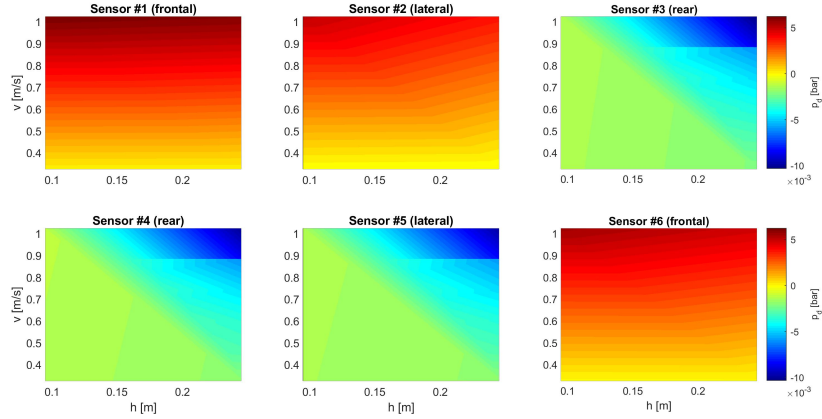


Figure 19: Overpressure p_d at each sensor as a function of the flow characteristics h and v . Flow incidence: $\theta = 45^\circ$.

515 wall and the negative values at the lateral and rear walls correspond to the
free-surface evolution, which is mainly characterized by a water-level increase
at the front wall, a water-level decrease at the lateral walls and a slightly lower
decrease at the rear wall. Further, the water-level variation significantly affects
the upstream region, while the bottom boundary layer entails a threshold at the
520 lateral and rear walls (see section 3.1 and Figure 8). Conversely, the initial water
depth slightly affects the water level at the frontal surfaces, but significantly
changes at the lateral and downstream walls. In particular, the water surface
at the lateral walls significantly changes when the flow approaches the structure
with an angle, with a maximum gradient measured when $\theta = 45^\circ$.

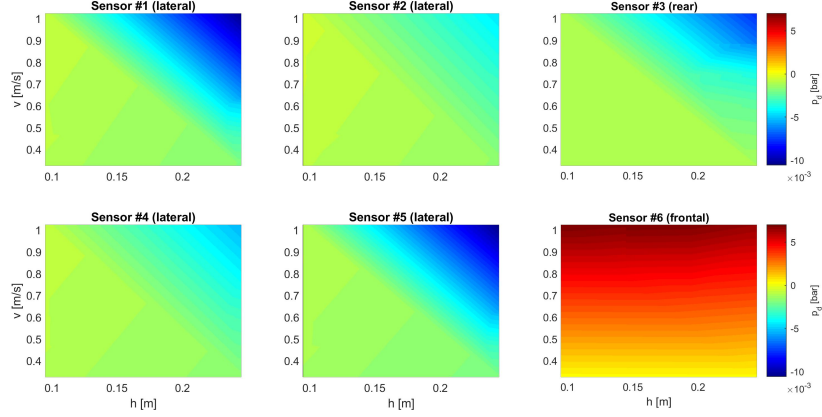


Figure 20: Overpressure p_d at each sensor as a function of the flow characteristics h and v . Flow incidence: $\theta = 90^\circ$.

525 The values of peak frequencies and peak periods evaluated with the spectral analysis for the “Fmax” case (Figure 6) and “Fmin” case (Figure 7), reported in section 2.2.2, suggest that large Froude numbers generate coherent structures/vortices characterized by time scales much smaller (i.e. velocity scales much larger) than those obtained with smaller Fr . Hence, as expected, the induced vorticity scales are in agreement with the flow dynamics around the building.

To further study the flood action on the building, some global indexes are evaluated, i.e. Fr and the drag coefficient C_D , which characterize the flow and the flow-building interaction. The approach used by Qi et al. (2014) is followed, where a force balance is applied exploiting a simple one-dimensional model.

535 The specific momentum flux plus the specific hydrostatic pressure needs to be conserved along the flume, i.e.

$$S_1 = S_2, \quad (2)$$

where S_1 is the force in correspondence of the impact wall, which is equated to the force in steady-flow condition S_2 , i.e. those characterizing a region located far downstream from the structure, where the flow field is almost uniform and one-dimensional. The forces are estimated as:

$$S_i = u_i^2 h_i + \frac{1}{2} g h_i^2, \quad (3)$$

with h_i and u_i being, respectively, the water depth and velocity at the i -th section ($i = 1, 2$), while g is the gravity acceleration. It can be assumed that far downstream from the structure, the uniform flow conditions are recreated, i.e. $h_2 \equiv h$ and $u_2 \equiv v$ (see left panels of Figure 3). The water depth at the impact surface h_1 can be retrieved using the total pressure p_t , i.e. $h_1 = p_t / \rho g + d_s$, where $d_s = 7.5\text{cm}$ is the vertical distance between each sensor and the reference bed.

Use of eq. 3 gives the forces at the downstream and upstream section

$$S_2 = v^2 h + \frac{1}{2} g h^2, \quad (4)$$

550

$$S_1 = v^2 \left(\frac{p_t}{\rho} g + d_s \right) + \frac{1}{2} g \left(\frac{p_t}{\rho} g + d_s \right)^2, \quad (5)$$

Substitution of equations 4 and 5 in eq. 2 leads to the velocity at the upstream section:

$$u_1 = \sqrt{\frac{S_2 - \frac{1}{2} g h_1^2}{h_1}}. \quad (6)$$

The velocities at the upstream section u_1 are used to evaluate the corresponding Froude number (Fr_1), which is plotted against the Froude number far from the structure (Fr_2 , evaluated with v , i.e. $Fr_2 = Fr$) in Figure 21, as in Qi et al. (2014). Notice that some discrepancies exist between the one-dimensional model used for the reconstruction and the flow field three-dimensionality experienced in the flume, mainly observed with small depths. Hence, the results are only shown for larger depths, i.e. $h = (0.145 \div 0.245)m$, and for cases during which the flow was perpendicular to the impact wall, i.e. $\theta = 0^\circ$ and $\theta = 90^\circ$.

560

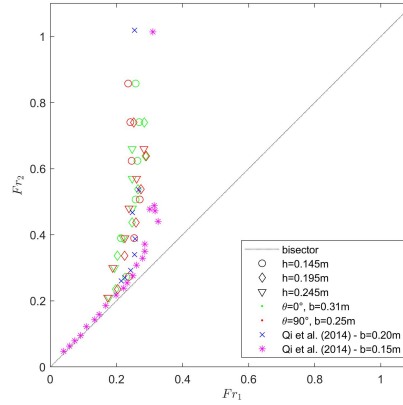


Figure 21: Fr_1 versus Fr_2 obtained from the one-dimensional model of eq. 2. Flow incidence: $\theta = 0^\circ$ (green) and $\theta = 90^\circ$ (red). Water depths: $h = 0.145m$ (\circ), $h = 0.195m$ (\diamond), $h = 0.245m$ (∇).

As already stated and demonstrated (e.g., Brocchini and Peregrine, 2001; Qi et al., 2014), low flow conditions provide $Fr_1 \approx Fr_2$ (values around 0.2–0.3 are close to the bisector), while larger flow conditions (Fr_2 increase) generate an almost constant Fr_1 value. An important blocking effect exists, with the tested blocking ratio $b/w = 0.25$ (red symbols) and 0.31 (green symbols) leading to a change at small Froude numbers in the data distribution, i.e. from $Fr_1 \approx Fr_2$ to $Fr_1 \approx \text{constant}$.

565

To check the validity of the present results, a comparison with Qi et al. (2014) is shown in Figure 21. Specifically, the data referring to the cases characterized by the largest tested blocking ratios ($b/w = 0.20$ and $b/w = 0.15$) are plotted. Although the points referring to $b/w = 0.20$ may be expected to fall on the right of, and not within, the data referring to the present tests (characterized by larger values of b/w), such behavior is due to the different nature of the experiments. However, despite the differences in the experimental methodology (non-inertial instead of inertial approach) and in the used materials (masonry walls instead of smooth walls), as well as in the used geometrical scale, such comparison confirms that the global hydrodynamics induced by the interaction between the moving building and the water at rest is well reproduced in the present tests.

An overall behavior of the experimental tests can be obtained from the analysis of the water level variations between upstream (frontal sensors) and downstream (rear sensors) of the structure. To this aim, the overpressure measured at each sensor location has been used to find the water level variation, as $\Delta\eta = (p_{d,up} - p_{d,dn})/\rho g$, where $p_{d,up}$ and $p_{d,dn}$ are, respectively, the upstream overpressure (e.g., that measured by sensors 1 and 2 when $\theta = 0^\circ$) and downstream overpressure (e.g., measured by sensors 4 and 5 when $\theta = 0^\circ$). The law presented by Fenton (2003)

$$\Delta\eta = \frac{v^2}{2g} \frac{C_D}{|\beta Fr^2 - 1|} \frac{b}{w} \quad (7)$$

is valid when the momentum flux does not significantly change between the upstream and downstream sections of either completely or partly submerged obstacles (e.g., bridge piers, logs). Assuming that the Boussinesq coefficient $\beta \approx 1$, the drag coefficient can be obtained as

$$C_D = \frac{\Delta\eta}{v^2/2g} \frac{|Fr^2 - 1|}{b/w}. \quad (8)$$

Figure 22 illustrates the dependence on Fr of the measured $\Delta\eta$ in both dimensional (top panel) and dimensionless (middle panel) forms. Here, with the aim to summarize all findings, all tested angles have been included. In the cases characterized by $0^\circ < \theta < 90^\circ$, a suitable impact surface has been accounted for, hence a suitable width b (see the legend), while $\Delta\eta$ has been calculated using the measurements from the more upstream ($p_{d,up}$) and downstream ($p_{d,dn}$) sensors. All configurations characterized by subcritical flow conditions ($Fr \leq 1$) are represented. The dimensionless data are almost aligned along a polynomial best-fit law ($R^2 = 0.854$), almost independently of the flow incidence, i.e. of the structure shape. Similarly, the reconstructed drag coefficient (bottom panel) reveals the slight dependence of C_D on the flow incidence, providing a fairly good alignment along the best-fit curve ($R^2 = 0.853$).

The values obtained for the drag coefficient are always lower than those commonly suggested by the literature, where $C_D = 1.9 \div 2$ (e.g., Cuomo et al., 2008; Qi et al., 2014; Sarjamee et al., 2017). This suggests that the drag force,

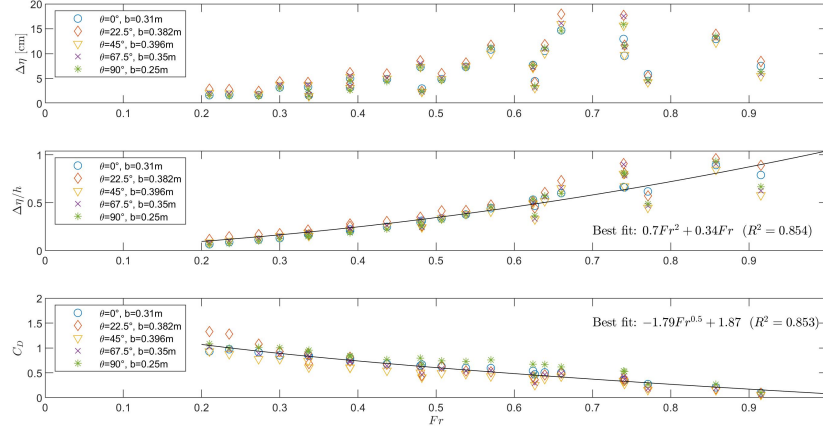


Figure 22: Evolution with Fr of the dimensional water level variation $\Delta\eta$ (top), the dimensionless water level variation $\Delta\eta/h$ (middle) and the reconstructed drag coefficient C_D (bottom).

which is typically used for damage-assessment purposes, is significantly larger than what expected, and this may also depend on the construction type studied in the present work, i.e. masonry building. Similarly, the observed hydrodynamics (e.g., the water-level variation $\Delta\eta$) are affected by the building-model characteristics, like the roughness reproduced using clay-bricks and mortar.

Analytical formulations, commonly used for the prediction of the backwater profile upstream of bridge piers, suggest similar $\Delta\eta$ values. As an example, application of empirical laws valid for rectangular channels (e.g., Atabay et al., 2018) to the case with $\theta = 0^\circ$, $v = 1.023\text{m/s}$ and $h = 0.245\text{m}$, leads to $\Delta\eta_{an} = 10.5\text{cm}$, which suitably compares with the experimental value $\Delta\eta = 14.7\text{cm}$.

In addition, preliminary numerical results, obtained using ANSYS Fluent and exploiting an inertial reference frame, i.e. a water flow impacting a fixed structure, confirm the validity of the experimental approach used in the present work. In particular, for the above-mentioned case, highly comparable results are found at the frontal wall, with differences of $\approx 1\%$ between measured and simulated p_d . Furthermore, both water-level variation and drag coefficient (Figure 22), estimated using frontal and rear sensors, lead to differences smaller than 25% (e.g., the numerical result $\Delta\eta_{num} = 19.1\text{cm}$ suitably compares with the experimental value $\Delta\eta = 14.7\text{cm}$). Differences partially depend on the discrepancies existing in the numerical representation of the experimental setu (e.g. the wall friction). Further details will be provided in a dedicated work, aimed at investigating both numerical-experimental comparison and aspects concerning the hydrodynamics around buildings subjected to angled flows.

Finally, this work: i) allows one to estimate both drag coefficient and water level around a masonry building, based on use of the input flood character-

istics (see middle and bottom panels of Fig. 22), which may help, e.g., local
 authorities to predict the impact of flood waters on the urban environment,
 even when building walls are not parallel nor perpendicular to the main flow
 direction or when a specific blocking ratio exists (Fig. 1); ii) illustrates the
 role of the building-flow relative angle, never studied before, to the authors'
 knowledge, which is suggested to have a weak influence on the drag coefficient;
 iii) suggests the suitability to carry out experimental tests using a non-inertial
 approach, which leads to global results comparable to those obtained using tra-
 ditional approaches; iv) enables one to evaluate the possible activation of various
 mechanisms.

5. Conclusions

This paper presents the main results of a study carried out in the Laboratory
 of Hydraulics and Maritime Constructions of the Università Politecnica delle
 Marche (Italy), using a geometric scaled (1:10) masonry building dragged in
 the water at rest by a trolley. In a non-inertial reference frame, such model
 represents a building impacted by flood waters.

The effect of different flow characteristics on the hydrodynamics around the
 impacted building is here analyzed, hence several tests have been carried out and
 some of the main parameters, i.e. still water depth, flow velocity and incidence
 angle, have been varied. The work underlines that all such parameters play an
 important role on the pressure acting at the building walls.

At the impacted wall, the velocity provides significant variations in both
 overpressure and water super-elevation, while the initial water depth does not
 provide significant changes. At the lateral and rear walls, both depth and ve-
 locity play an important role and provide large overpressure/super-elevation
 changes.

The flow incidence angle also significantly affects the overpressure and the
 consequent hydrodynamics around the structure. In particular, a wall impacted
 by an inclined flow experiences different pressure fields: (i) when the flow is
 perpendicular, the wall is subject to a large positive overpressure and water-
 level increase, almost constant throughout the wall width; (ii) when the flow
 changes from perpendicular to 45° , an overpressure/free-surface gradient gen-
 erates along the wall, with the largest gradient occurring at 45° ; (iii) when the
 flow is tangent to the wall, a negative overpressure generates, associated to a
 water-level decrease.

Different flow regimes (Fr numbers) provide different flow behaviors when
 the flow-structure angle changes, this also depending on the blocking effect.
 This is fundamental in terms of the flow regimes generating upstream and down-
 stream of the structure, i.e. existence of neighborhoods and close buildings lead
 to a larger overpressure/super-elevation with respect to isolated structures, this
 being confirmed in both recent literature and present experiments.

Application of literature formulas to the subcritical flow cases enabled to
 find an increasing trend of the dimensionless water-level variation, estimated

675 using the upstream and downstream water levels, with Fr . A further trend is found for the drag coefficient, which decreases with Fr . Such findings refer to all experimental tests, hence they are valid for all angles and blocking ratios.

Finally, the presented results underline that the knowledge of the main input flood conditions (water depth, flow velocity, flow direction) may help one in
680 hindcasting/predicting the hydrodynamic actions and the activation of possible mechanisms on buildings characterized by either specific angles with respect to the main flow or blocking ratios, as typical of urban fabrics worldwide. Such points are crucial in real-world applications, especially when dealing with the urban environment, where the hydrodynamics is highly complex.

685 Accounting for the above aspects and use of the proposed laws will thus help authorities when dealing with urban planning or evacuation-strategy plans, which also involve pedestrian safety during floods.

Acknowledgements

This work is fully supported by the scientific project “Building Resilience to flood Impact Deriving from Global warming in Europe (BRIDGE)” funded
690 by Università Politecnica delle Marche, internal program 2017/2018. Special thanks go to Prof. M. Brocchini, for his helpful and useful suggestions, as well as to Dr. G. Di Giovine and Mr. L. Luccarini, for designing and realizing the experimental apparatus.

695 References

- AASHTO, . AASHTO LRFD Bridge Design Specification. American Association of State Highway and Transportation Officials; Washington DC; 6th ed.; 2013. .
- Almasri, A., Moqbel, S.. Numerical evaluation of aashto drag force coefficients of water flow around bridge piers. Journal of Engineering Materials and
700 Technology 2017;139:021001. doi:10.1115/1.4035253.
- Árnason, H.. Interactions between an incident bore and a free-standing coastal structure. Ph.D. thesis; University of Washington, Seattle, WA; 2005.
- Arnell, N.W., Gosling, S.N.. The impacts of climate change on river flood risk at the global scale. Climatic Change 2016;134(3):387–401.
705
- Arrighi, C., Alcèrrec-Huerta, J., Oumeraci, H., Castelli, F.. Drag and lift contribution to the incipient motion of partly submerged flooded vehicles. Journal of Fluids and Structures 2015;57:170–184.
- Atabay, S., Haji Amou Assar, K., Hashemi, M., Dib, M.. Prediction of the backwater level due to bridge constriction in waterways. Water and Environ-
710 ment Journal 2018;32(1):94–103.

- Azinfar, H., Kells, J.A.. Flow resistance due to a single spur dike in an open channel. *Journal of Hydraulic research* 2009;47(6):755–763.
- 715 Bernardini, G., Postacchini, M., Quagliarini, E., Brocchini, M., Cianca, C., D’Orazio, M.. A preliminary combined simulation tool for the risk assessment of pedestrians flood-induced evacuation. *Environmental Modelling & Software* 2017;96:14–29.
- 720 Braun, B., Aßheuer, T.. Floods in megacity environments: vulnerability and coping strategies of slum dwellers in dhaka/bangladesh. *Natural hazards* 2011;58(2):771–787.
- Brocchini, M., Peregrine, D.. The dynamics of strong turbulence at free surfaces. part 1. description. *Journal of Fluid Mechanics* 2001;449:225–254.
- 725 Charvet, I., Ioannou, I., Rossetto, T., Suppasri, A., Imamura, F.. Empirical fragility assessment of buildings affected by the 2011 great east japan tsunami using improved statistical models. *Natural Hazards* 2014;73(2):951–973.
- Chow, V.T.. *Open-channel hydraulics*. volume 1. McGraw-Hill New York, 1959.
- 730 Cuomo, G., Shams, G., Jonkman, S., van Gelder, P.. Hydrodynamic loadings of buildings in floods. In: *Coastal Engineering 2008 - 31st International Conference*. 2008. doi:10.1142/9789814277426_0310.
- Custer, R., Nishijima, K.. Flood vulnerability assessment of residential buildings by explicit damage process modelling. *Natural Hazards* 2015;78(1):461–496.
- 735 Debus, K., Berkoe, J., Rosendall, B., Shakib, F.. Computational fluid dynamics model for tacoma narrows bridge upgrade project. In: *ASME/JSME 2003 4th Joint Fluids Summer Engineering Conference*. American Society of Mechanical Engineers; 2003. p. 179–184.
- 740 Diakakis, M., Andreadakis, E., Nikolopoulos, E., Spyrou, N., Gogou, M., Deligiannakis, G., Katsetsiadou, N., Antoniadis, Z., Melaki, M., Georgakopoulos, A., et al. An integrated approach of ground and aerial observations in flash flood disaster investigations. the case of the 2017 mandra flash flood in greece. *International Journal of Disaster Risk Reduction* 2019;33:290–309.
- 745 Dutta, S., Panigrahi, P., Muralidhar, K.. Experimental investigation of flow past a square cylinder at an angle of incidence. *Journal of engineering mechanics* 2008;134(9):788–803.
- 750 Duy, P., Chapman, L., Tight, M., Thuong, L., Linh, P.. Urban resilience to floods in coastal cities: Challenges and opportunities for ho chi minh city and other emerging cities in southeast asia. *Journal of Urban Planning and Development* 2017;144(1):05017018.

- Faccini, F., Paliaga, G., Piana, P., Sacchini, A., Watkins, C.. The bisagno stream catchment (genoa, italy) and its major floods: geomorphic and land use variations in the last three centuries. *Geomorphology* 2016;273:14–27.
- 755 FEMA, . Coastal construction manual: Principles and practices of planning, siting, designing, constructing, and maintaining residential buildings in coastal areas, fema p-55. 2011.
- Fenton, J.. The effects of obstacles on surface levels and boundary resistance in open channels 2003;.
- 760 Haehnel, R.B., Daly, S.F.. Maximum Impact Force of Woody Debris on Floodplain Structure. Technical Report; U.S. Army Engineer Research and Development Center Cold Regions Research and Engineering Laboratory; 2002.
- Haehnel, R.B., Daly, S.F.. Maximum impact force of woody debris on floodplain structures. *Journal of Hydraulic Engineering* 2004;130:112–120. doi:10.1061/~ASCE!0733-9429~2004!130:2~112!
- 765 Halgamuge, M.N., Nirmalathas, A.. Analysis of large flood events: Based on flood data during 1985–2016 in australia and india. *International Journal of Disaster Risk Reduction* 2017;24:1–11.
- Heddleson, C., Brown, D., Cliffe, R.. Summary of drag coefficients of various shaped cylinders. Technical Report; GENERAL ELECTRIC CO CINCINNATI OH; 1957.
- 770 Huizinga, J., de Moel, H., Szewczyk, W.. Global flood depth-damage functions. Methodology and the database with guidelines. Technical Report; EUR 28552 EN; 2017. doi:10.2760/16510.
- Kelman, I., Spence, R.. An overview of flood actions on buildings. *Engineering Geology* 2004;73(3-4):297–309.
- 775 Kundzewicz, Z.W., Kanae, S., Seneviratne, S.I., Handmer, J., Nicholls, N., Peduzzi, P., Mechler, R., Bouwer, L.M., Arnell, N., Mach, K., et al. Flood risk and climate change: global and regional perspectives. *Hydrological Sciences Journal* 2014;59(1):1–28.
- 780 Lee, E.H., Kim, J.H.. Development of a flood-damage-based flood forecasting technique. *Journal of Hydrology* 2018;.
- Liang, Q., cui Chen, K., Hou, J., Xiong, Y., Wang, G., Qiang, J.. Hydrodynamic modelling of flow impact on structures under extreme flow conditions. *Journal of Hydrodynamics* 2016;28(2):267–274. doi:10.1016/S1001-6058(16)60628-5.
- 785 Lindsey, W.F.. Drag of cylinders of simple shapes 1938;.

- Lorenzoni, C., Postacchini, M., Brocchini, M., Mancinelli, A.. Experimental study of the short-term efficiency of different breakwater configurations on beach protection. *Journal of Ocean Engineering and Marine Energy* 2016;2(2):195–210.
- 790 Lorenzoni, C., Soldini, L., Brocchini, M., Mancinelli, A., Postacchini, M., Seta, E., Corvaro, S.. Working of defense coastal structures dissipating by macroroughness. *Journal of waterway, port, coastal, and ocean engineering* 2010;136(2):79–90.
- 795 Memmola, F., Darvini, G.. Changes in precipitation-runoff relationship in six catchments of the adriatic coast of center italy. In: *Proceedings of 13th International Conference on Hydroinformatics*. 2018. .
- Miozzi, M., Postacchini, M., Corvaro, S., Brocchini, M.. Whole-wavelength description of a wave boundary layer over permeable wall. *Experiments in Fluids* 2015;56(6):127.
- 800 de Moel, H., van Alphen, J., Aerts, J.. Flood maps in europe—methods, availability and use. *Nat Hazards Earth Syst Sci* 2009;9:289–301.
- Nasim, M., Setunge, S., Zhou, S., Mohseni, H.. An investigation of water-flow pressure distribution on bridge piers under flood loading. *Structure and Infrastructure Engineering* 2018;;1–11.
- 805 Nistor, I., Palermo, D., Cornett, A., Al-Faesly, T.. Experimental and numerical modeling of tsunami loading on structures. In: *Coastal Engineering Proceedings*. volume 32; 2010. doi:10.9753/icce.v32.currents.2.
- Petrone, C., Rossetto, T., Goda, K.. Fragility assessment of a rc structure under tsunami actions via nonlinear static and dynamic analyses. *Engineering Structures* 2017;136:36–53.
- 810 Pistrika, A., Tsakiris, G., Nalbantis, I.. Flood depth-damage functions for built environment. *Environmental Processes* 2014;1(4):553–572.
- Pistrika, A.K., Jonkman, S.N.. Damage to residential buildings due to flooding of new orleans after hurricane katrina. *Natural Hazards* 2010;54(2):413–434.
- 815 Poff, N.L., Brown, C.M., Grantham, T.E., Matthews, J.H., Palmer, M.A., Spence, C.M., Wilby, R.L., Haasnoot, M., Mendoza, G.F., Dominique, K.C., et al. Sustainable water management under future uncertainty with eco-engineering decision scaling. *Nature Climate Change* 2016;6(1):25.
- 820 Qi, Z., Eames, I., Johnson, E.. Force acting on a square cylinder fixed in a free-surface channel flow. *Journal of Fluid Mechanics* 2014;756:716–727.
- Ranasinghe, R., Duong, T.M., Uhlenbrook, S., Roelvink, D., Stive, M.. Climate-change impact assessment for inlet-interrupted coastlines. *Nature Climate Change* 2013;3(1):83.

- 825 Ranga Raju, K., Rana, O., Asawa, G., Pillai, A.. Rational assessment
of blockage effect in channel flow past smooth circular cylinders. *Journal of
Hydraulic Research* 1983;21(4):289–302.
- Raynaud, D., Thielen, J., Salamon, P., Burek, P., Anquetin, S., Alfieri, L..
A dynamic runoff co-efficient to improve flash flood early warning in europe:
830 evaluation on the 2013 central european floods in germany. *Meteorological
Applications* 2015;22(3):410–418.
- Robertson, I.N., Riggs, H.R., Yim, S.C.S., Young, Y.L.. Lessons from
hurricane katrina storm surge on bridges and buildings. *Journal of Waterway,
Port, Coastal, and Ocean Engineering* 2007;133(6):463–483.
- 835 Roshko, A.. On the wake and drag of bluff bodies. *Journal of the aeronautical
sciences* 1955;22(2):124–132.
- Saharia, M., Kirstetter, P.E., Vergara, H., Gourley, J.J., Hong, Y.. Character-
ization of floods in the united states. *Journal of Hydrology* 2017;548:524–535.
- 840 Sarjamee, S., Nistor, I., Mohammadian, A.. Numerical investigation of
the influence of extreme hydrodynamic forces on the geometry of struc-
tures using openfoam. *Natural Hazards* 2017;87:213235. doi:10.1007/
s11069-017-2760-3.
- Schlichting, H., et al. *Boundary-layer theory*. Springer, 1974.
- Soares-Frazão, S., Zech, Y.. Dam-break flow through an idealised city. *Journal*
845 *of Hydraulic Research* 2008;46(5):648–658.
- Soldini, L., Darvini, G.. Extreme rainfall statistics in the marche region, italy.
Hydrology Research 2017;48(3):686–700.
- Suppasri, A., Mas, E., Charvet, I., Gunasekera, R., Imai, K., Fukutani,
Y., Abe, Y., Imamura, F.. Building damage characteristics based on sur-
veyed data and fragility curves of the 2011 great east japan tsunami. *Natural*
850 *Hazards* 2013;66(2):319–341.
- Villatoro, M., Silva, R., Méndez, F., Zanuttigh, B., Pan, S., Trifonova, E.,
Losada, I., Izaguirre, C., Simmonds, D., Reeve, D., et al. An approach
to assess flooding and erosion risk for open beaches in a changing climate.
855 *Coastal Engineering* 2014;87:50–76.
- Wang, Y.h., Zou, Y.s., Xu, L.q., Luo, Z.. Analysis of water flow pressure
on bridge piers considering the impact effect. *Mathematical Problems in
Engineering* 2015;2015.
- 860 Xiao, S., Li, H., M., . Impact of flood on a simple masonry building. *Journal
of Performance of Constructed Facilities* 2013;27(5):550–563. doi:10.1061/
(ASCE)CF.1943-5509.0000357.
- Yoon, D.H., Yang, K.S., Choi, C.B.. Flow past a square cylinder with an
angle of incidence. *Physics of fluids* 2010;22(4):043603.